Chinese Journal of
POLYMER SCIENCE

RESEARCH ARTICLE

https://doi.org/10.1007/s10118-026-3626-5
Chinese J. Polym. Sci. **2026**, *44*, 2331–2340

Molecular Weight Distribution Effects on the Structural and Mechanical Performance of Conjugated Polymers Incorporating Flexible Spacers: A Simulation Study

Hai-Yan Weng[a], Ji-Yuan Xing[b], Rui Shi[a*], and Zhong-Yuan Lu[a*]

[a] *State Key Laboratory of Supramolecular Structure and Materials, Institute of Theoretical Chemistry, Jilin University, Changchun 130023, China*
[b] *State Key Laboratory of Electroanalytical Chemistry, Changchun Institute of Applied Chemistry, Chinese Academy of Sciences, Changchun 130023, China*

Electronic Supplementary Information

Abstract Conjugated polymers incorporating flexible spacers (CP-FSs) offer a promising route to mechanically robust active layers for flexible organic solar cells. However, the influence of molecular weight distribution (MWD)—a fundamental polymer characteristic—on structural and mechanical performance remains poorly understood due to synthetic challenges. Here, we employ dissipative particle dynamics and coarse-grained molecular dynamics simulations to elucidate how MWD, quantified by polydispersity index (PDI), governs structure-property relationships in CP-FSs. Our results reveal that PDI acts as a molecular switch controlling phase morphology: increasing PDI drives transitions from lamellar to perforated lamellar structures at intermediate rigid segment lengths. At the molecular level, higher PDI significantly increases the fraction of bridging conformations (v_{bridge}), strengthening a load-bearing network. During tensile deformation, this enhanced load-bearing network suppresses destructive fibrillation and instead promotes reconstructive strengthening through dynamic loop-to-bridge transitions. These findings demonstrate that controlled MWD offers a composition-independent strategy for developing mechanically robust active layers, providing practical guidelines for flexible organic solar cell design.

Keywords Conjugated polymers incorporating flexible spacers; Molecular weight distribution; Structural performance; Mechanical performance

Citation: Weng, H. Y.; Xing, J. Y.; Shi, R.; Lu, Z. Y. Molecular weight distribution effects on the structural and mechanical performance of conjugated polymers incorporating flexible spacers: a simulation study. *Chinese J. Polym. Sci.* **2026**, *44*, 2331–2340.

INTRODUCTION

Flexible organic solar cells (FOSCs) hold tremendous promise for applications in wearable electronics, portable devices, and building-integrated photovoltaics,[1–3] owing to their unique combination of flexibility, light weight, and compatibility with large-area manufacturing.[4,5] However, their widespread commercial deployment remains limited by strain-induced mechanical failure within the active layer. Consequently, developing active layer materials that deliver both high power conversion efficiency and exceptional mechanical durability to withstand structural damage and minimize strain-induced performance degradation has become imperative.[6,7] Conjugated polymers (CPs), the predominant active layer materials, possess highly rigid backbones with strong π-π interactions that enable efficient charge transport pathways essential for high power conversion efficiency.[8,9] Yet this inherent backbone rigidity severely constrains chain segment mobility, preventing effective stress dissipation through mechanisms such as chain slippage and conformational rearrangements during deformation.[10,11] This limited plastic deformation capacity prevents efficient relief of localized stress concentrations, promoting crack initiation and propagation that ultimately lead to mechanical failure.[12] Therefore, overcoming the intrinsic brittleness of CPs is crucial for achieving mechanically robust FOSC applications.

Molecular engineering strategies have proven highly effective in addressing the inherent brittleness of CPs.[13–15] Among these approaches, conjugated polymers incorporating flexible spacers (CP-FSs), designed following the "rigid-flexible synergy" principle, offer compelling advantages: rigid conjugated segments preserve the π-π stacking network essential for charge transport, while flexible spacers enhance mechanical properties by enabling energy dissipation through conformational adjustments, as demonstrated in recent experimental studies.[16–20] However, CP-FS mechanical properties depend not only on chemical structure but also critically on self-assembly structures spanning multiple length scales.[21–23] Specifically, (i) molecular chain arrangement (crystallinity and orientation) determines fundamental material rigidity and strength;[16,24] (ii) chain entanglement degree governs toughness, ductility, and crack propagation

* Corresponding authors, E-mail: shirui816@jlu.edu.cn (R.S.)
E-mail: luzhy@jlu.edu.cn (Z.Y.L.)
Received February 15, 2026; Accepted March 12, 2026; Published online May 28, 2026

resistance;[25] and (iii) phase-separated morphology (domain size and purity) directly affects stress distribution, transfer, and potential interfacial failure modes.[26] Understanding the factors controlling these structures is therefore essential for optimizing CP-FS mechanical performance. Molecular weight distribution (MWD) represents a fundamental intrinsic property of CPs that profoundly influences structures.[27,28] Understanding how MWD modulates these structures provides the foundation for interpreting other variables' effects. Crucially, MWD can be adjusted without altering chemical composition, offering a straightforward yet powerful approach for optimizing mechanical properties. For example, increasing molecular weight enhances polymer chain entanglement, thereby improving material toughness.[29] However, MWD's role in controlling CP-FS structural and mechanical properties remains largely unexplored. This knowledge gap stems primarily from inherent synthetic limitations. Stille polycondensation, the predominant CP-FS synthesis route,[16–18,24–26,30] exhibits high sensitivity to reaction conditions and susceptibility to side reactions, typically producing CP-FSs with broad, poorly controlled, and batch-variable MWDs.[31,32] This experimental irreproducibility severely impedes establishing clear structure-property relationships, fundamentally constraining opportunities for rational molecular design to tailor mechanical properties.

In this work, we overcome experimental limitations in controlling CP-FS MWD through computational simulations.[33–35] We develop coarse-grained CP-FS models following Flory-Schulz chain length distributions and employ an integrated simulation framework combining dissipative particle dynamics (DPD) and coarse-grained molecular dynamics (CGMD). This approach enables us to elucidate how MWD, quantified by the polydispersity index (PDI), governs multiscale structures including phase morphology and chain conformation, while tracking structural evolution under deformation. Remarkably, we demonstrate that PDI acts as a molecular switch, transforming the mechanical response from destructive fibrillation to reconstructive strengthening of three-dimensional perforated lamellar structures. Our study provides fundamental insights into CP-FS structure-property relationships, establishing theoretical guidelines for the rational design of mechanically robust active layer materials for FOSCs with enhanced practical performance potential.

MODEL AND SIMULATION DETAILS

We developed a coarse-grained model to represent CP-FSs, as schematically illustrated in Fig. 1(a). In this model, each rigid conjugated segment is depicted as a green rod block of k bonded particles, while each flexible spacer is represented as a blue coil block of l bonded particles. A single polymer chain comprises n rod-coil repeating units, denoted $(R_kC_l)_n$, where n is the degree of polymerization (DP). To isolate the effect of the molecular weight distribution (MWD), we held k and l constant for all chains in each system and then varied the MWD by adjusting the number of chains at each DP while keeping the total particle count fixed.

Under ideal conditions of uniform monomer reactivity and no side reactions, Stille polycondensation follows step-growth kinetics, producing an MWD described by the Flory-Schulz distribution.[36] We therefore adopted the discrete form

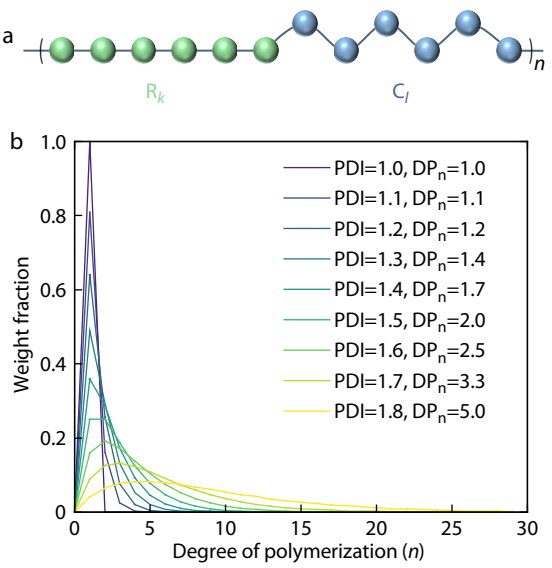

Fig. 1 (a) Schematic illustration of the coarse-grained model for a conjugated polymer with flexible spacers, $(R_kC_l)_n$. The rigid conjugated segment is shown as a green rod block of k particles; the flexible spacer is a blue coil block of l particles. Each chain contains n rod-coil units. (b) Molecular weight distribution (MWD) curves of $(R_kC_l)_n$ with polydispersity index (PDI) values from 1.0 to 1.8, based on the discrete Flory-Schulz distribution. In each case, k and l are fixed, and the MWD is tuned by altering the number of chains at each DP while maintaining a constant total particle count. The corresponding number-average DP (DP_n) for each PDI is given in the legend.

$$W_n = np^{n-1}(1-p)^2 \quad (1)$$

where W_n is the weight fraction of chains with DP = n and p is the extent of reaction. From this distribution, one obtains the number-average DP, $DP_n = 1/(1-p)$, and the polydispersity index, PDI = $1 + p$, both of which increase monotonically with p. For clarity, PDI serves as the primary descriptor in our study: different PDI values correspond to different p, yielding distinct MWD profiles and the associated DP_n. To construct systems that conform to the discrete Flory-Schulz distribution, a protocol involving truncation, renormalization, and nearest-integer rounding was employed. Specifically, the distribution was truncated at n=29. Even for the system with PDI=1.8, which contains the largest proportion of long-chain components, this limit still accounts for 98.95% of the total theoretical mass (Fig. S1a in the electronic supplementary information, ESI). After renormalizing the weight fractions within the captured range, the required number of chains for each DP was determined by rounding the calculated values to the nearest integers. This protocol ensured high statistical fidelity, as confirmed by the close agreement between the target discrete distribution and the implemented distribution in the simulation box (Fig. S1b in ESI). The resulting MWD profiles in Fig. 1(b) capture the fundamental characteristics of polydisperse systems. As PDI increases, the distribution broadens, its peak shifts to higher DP, and the high-molecular-weight tail becomes more pronounced, illustrating the strong influence of PDI on MWD shape.

To investigate how PDI influences CP-FS self-assembly and

mechanical behavior, we employed a two-stage simulation protocol combining DPD and CGMD. In the first stage, DPD was used to exploit its computational efficiency and obtain equilibrium self-assembled structures for various PDI values. These equilibrated DPD configurations were then converted into CGMD models, after which we performed CGMD simulations to probe mechanical response.[35,37–39] This two-step DPD-to-CG approach greatly reduces the computational cost compared to generating equilibrated assemblies directly *via* CGMD. All simulation parameters and the DPD-CG conversion protocol are detailed in Sections S2–S4 (in ESI).

For mechanical testing, we applied uniaxial tensile deformation by stretching the equilibrated systems along the Z direction at a constant strain rate of $0.02\sigma/\tau$ (σ and τ are the CGMD length and time units, respectively), while simultaneously contracting the X and Y dimensions to maintain constant volume. Here, the strain is defined as $\varepsilon = (L_z - L_{z,0})/L_{z,0}$, where L_z and $L_{z,0}$ are the instantaneous and initial simulation box lengths, respectively. Simulations used a time step $\Delta t = 0.001$ and were performed at temperature $T = 1.0$ with a Nosé-Hoover thermostat. All runs were carried out in the PyGAMD package,[41,42] with five independent simulations for each system to ensure statistical reliability.

RESULTS AND DISCUSSION

We first investigated the influence of MWD on self-assembly behavior. A PDI-segment length k phase diagram for $(R_kC_l)_n$ systems was constructed using DPD simulations (Fig. 2a). PDI varied from 1.0 to 1.8 (in increments of 0.1) and k from 2 to 8 (in increments of 2), with $k = l$ to fix the rod-to-coil volume fraction and isolate the effects of k and PDI on phase behavior.

For short k, *e.g.*, $k = l = 2$, the system forms alternating (R_2C_2) copolymers. In this regime, microphase separation remains suppressed (disordered phase as shown in Fig. 2b) because each repulsive "block" spans only two monomers, so even a very high Flory-χ_{RC} cannot amplify into long-range compositional order: $\chi N_{eff} \simeq \chi \times 2$ drives repulsion only over two repeat units. At the same time, the extreme density of R–C junctions imposes a prohibitive interfacial free-energy penalty, and forming any appreciable domain thickness would require chains to stretch far beyond their unperturbed dimensions, incurring large entropic costs. Covalent connectivity further frustrates demixing by tethering strongly repelling segments within the same molecule, forcing highly interdigitated, locally disordered conformations rather than well-defined domains. Finally, since polydispersity only introduces fluctuations on n, which does not change the (R_2C_2) alternating behavior, the system remains in a statistically mixed, disordered state with various PDI.

With increasing k, the longer blocks enhance the driving force for microphase separation, and the growing rigidity contrast between rod and coil segments further reduces their

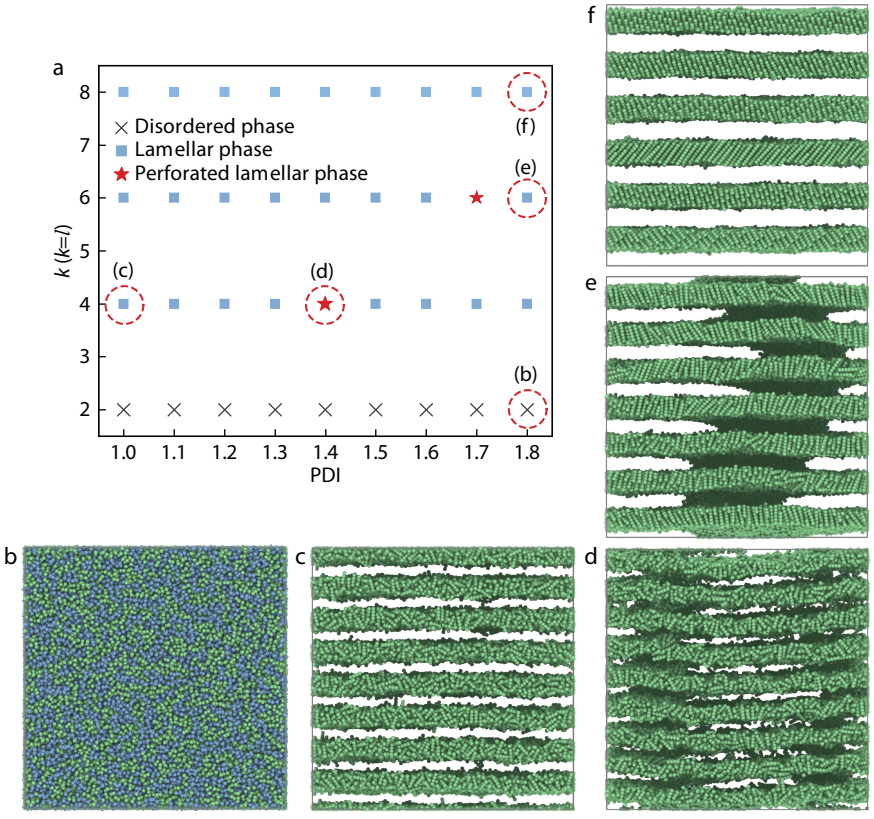

Fig. 2 (a) Self-assembly phase diagram of $(R_kC_l)_n$ as a function of the rigid segment length k and the polydispersity index (PDI). The coil length l was tuned with k to maintain a constant volume fraction. Five independent simulations were performed for each parameter set. (b–f) Representative snapshots corresponding to the points marked in (a), showcasing the distinct morphologies and the varying degrees of packing of the rod blocks. All snapshots were captured using the Open Visualization Tool (OVITO).[40]

https://doi.org/10.1007/s10118-026-3626-5

mutual miscibility. For $k = l = 4$ systems, lamellar (Lam) phases appear. Interestingly, the morphology depends strongly on PDI: at low PDI (1.0–1.3), narrow MWD yields nearly uniform domains and a single, well-defined lamellar spacing that balances low-curvature interfaces (minimizing interfacial area) and consistent domain thickness (minimizing chain stretching), as shown in Fig. 2(c). Once PDI exceeds 1.3, the broader MWD breaks this uniformity; some chains become overstretched while others are understretched, leading to packing frustration. Under the symmetric 1:1 rod-to-coil volume constraint, changing the global period is energetically costly, so the system relieves packing frustration by introducing localized curvature through perforations between lamellae (PL) (Fig. 2d), all the while preserving the average layer spacing. A quantitative distinction between Lam and PL is provided by the structure factor *S(q)* (Section S5 in ESI). These observations concur with established findings on how MWD drives structural adaptations to accommodate packing frustration and thereby disrupts long-range order.[43,44] Further extending rod block length to $k = l \geq 6$ triggers crystallization-like ordering within the rigid layers, as shown in Figs. 2(e) and 2(f). For $k = 6$, the parallel alignment of rods maximizes packing efficiency and produces exceptionally uniform, low-curvature interfaces, thereby stabilizing the Lam phase across a broad PDI window (1.0–1.6). Only when PDI exceeds about 1.6 does the increased chain-length heterogeneity become sufficient to induce perforated lamellae (Fig. 2e). At $k = 8$, the rod domains achieve even more perfect ordering (Fig. 2f), which quenches curvature fluctuations and preserves the Lam morphology throughout the entire PDI range explored (up to 1.8).

In summary, PDI governs phase behavior by introducing chain-length heterogeneity that disrupts uniform domain and drives localized curvature adjustments. However, its influence is strongly modulated by the rigid segment length k. Short blocks ($k = 2$) remain disordered regardless of PDI due to insufficient segregation strength, while intermediate blocks ($k = 4$) exhibit a clear PDI-dependent transition from lamellae to perforated lamellae. As k increases further ($k \geq 6$), crystallization-like ordering within the rod domains progressively suppresses curvature fluctuations, thereby raising or even eliminating the PDI threshold for perforation.

To elucidate how PDI-induced structural variations manifest in mechanical properties, we performed CGMD simulations of uniaxial tensile deformation on $(R_6C_6)_n$ systems across a range of PDI values. The $(R_6C_6)_n$ system was strategically chosen for its crystallization-like rod packing and its PDI-driven Lam-PL phase transition, providing an ideal platform to correlate morphological changes with mechanical response. Five representative systems were examined: four lamellar structures with PDI=1.0, 1.2, 1.5, and 1.6, and one perforated lamellar structure with PDI=1.8 system. The corresponding stress-strain curves, presented in Fig. 3 for strains up to 0.30, reveal a systematic evolution of mechanical behavior with increasing polydispersity. Notably, higher PDI values lead to more pronounced stress overshoots, accompanied by increases in both yield strain and yield stress. Furthermore, the post-yield stress softening becomes progressively more severe as PDI increases, indicating that chain-length

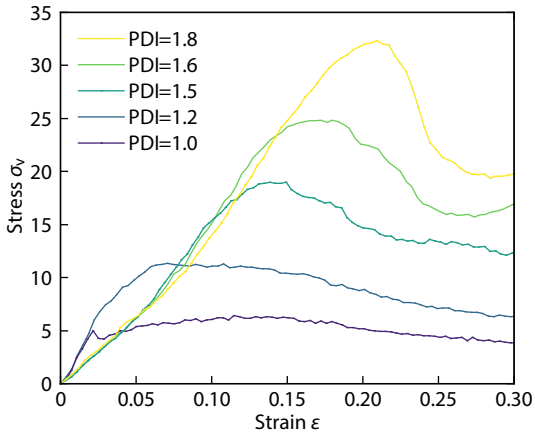

Fig. 3 Stress-strain curves for $(R_6C_6)_n$ systems with PDI values of 1.0, 1.2, 1.5, 1.6, and 1.8, over the strain range 0–0.30.

heterogeneity not only modifies the initial yielding behavior but also governs the extent of structural breakdown under deformation.

We conducted a comprehensive analysis of stress-strain responses and their associated structural transformations across the polydispersity spectrum. Since systems with PDI= 1.2 and 1.6 display mechanical and structural characteristics similar to those at PDI=1.0 and 1.5, respectively, we concentrate on three archetypal systems: monodisperse (PDI=1.0), moderately polydisperse (PDI=1.5), and highly polydisperse (PDI=1.8), as depicted in Fig. 4. Figs. 4(a), 4(g), and 4(m) display the stress-strain curves for the PDI=1.0, 1.5, and 1.8 systems, respectively, while panels (b)–(f), (h)–(l), and (n)–(r) chronicle their structural evolution at pivotal deformation stages. In the monodisperse system (PDI=1.0), uniform chain lengths promote the assembly of pristine lamellar structures (Fig. 4b), enabling efficient stress transmission and synchronized yielding. Upon reaching the yield point, these planar lamellae undergo coherent buckling, transforming into sinusoidal patterns (Fig. 4c). This collective instability triggers dramatic strain softening, evidenced by an abrupt stress decline. During softening, the buckled structures reconfigure into chevron-like domains *via* coordinated lamellar sliding and rotation (Fig. 4d). The ensuing stress plateau features pronounced fluctuations arising from repetitive cycles of domain fragmentation, rearrangement, and reorientation. With continued extension, these domains disintegrate into fibrillar assemblies that orient preferentially along the loading direction, while microvoids initiate at structural defects (inset, Fig. 4e). Eventually, void growth drives catastrophic failure (inset, Fig. 4f). This deformation sequence exemplifies a destructive mechanism whereby the pristine lamellar architecture collapses into disconnected fibrillar remnants. The moderately polydisperse system (PDI=1.5) exhibits a fundamentally different deformation mechanism characterized by structural reconstruction. Chain-length heterogeneity disrupts crystalline packing, yielding less-ordered initial lamellae (Fig. 4h) compared to the monodisperse case. Consequently, yielding transitions from collective buckling to distributed interfacial slip, generating localized disorder (Fig. 4i). The resulting strain softening is notably gentler than in the monodisperse system. During this phase, initially discrete lamellae progressively in-

https://doi.org/10.1007/s10118-026-3626-5

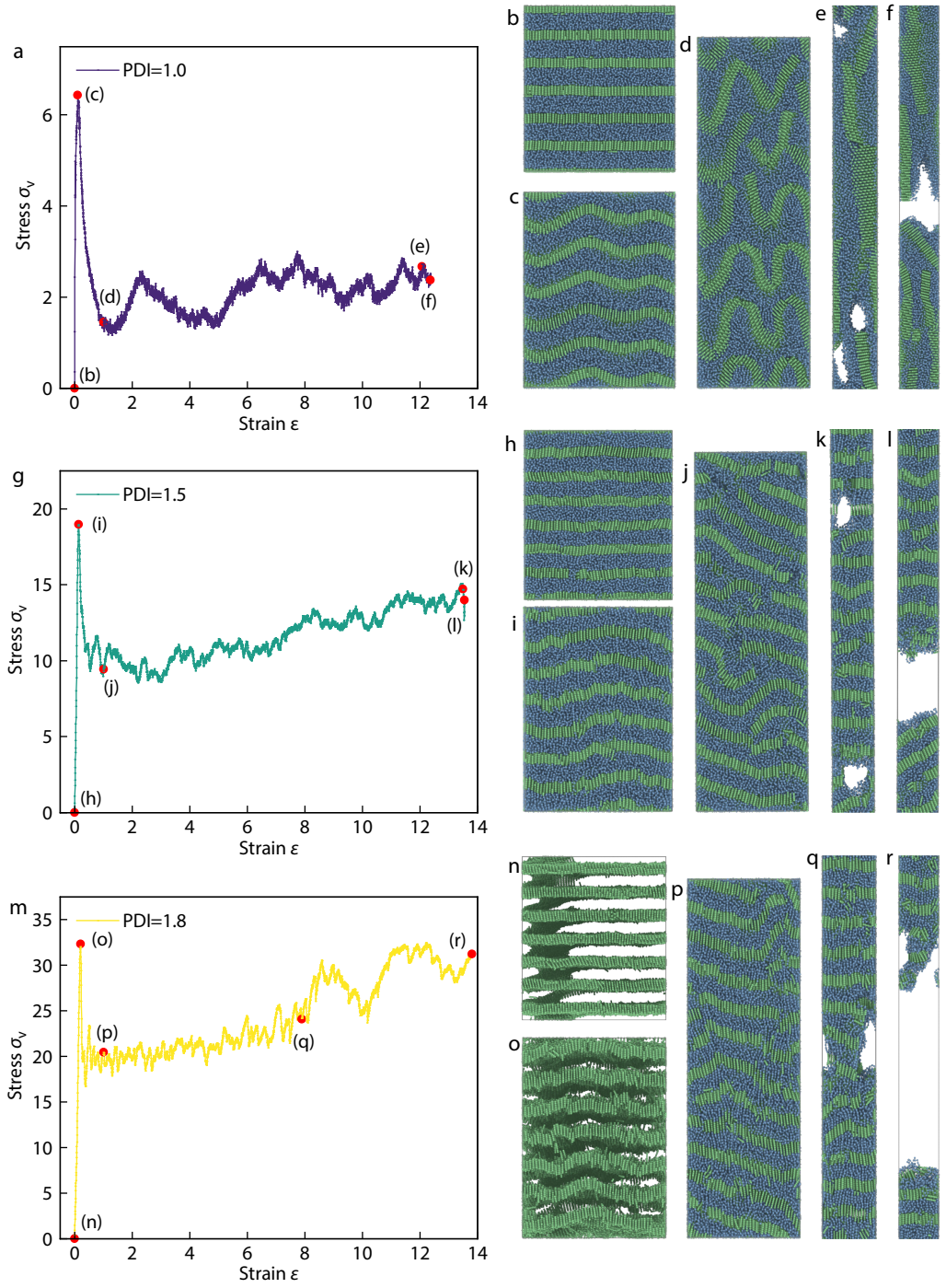

Fig. 4 Stress-strain curves for $(R_6C_6)_n$ systems with PDI values of 1.0, 1.5, and 1.8 are presented in panels (a), (g), and (m), respectively. Simulation snapshots, captured at the labeled points on these curves, are displayed in panels (b–f) for the PDI=1.0 system, (h–l) for the PDI=1.5 system, and (n–r) for PDI=1.8 system. In particular, panels (e, f), (k, l), and (q, r) provide close-up views of the fracture regions, highlighting the fracture process at large strains. The color scheme for the components in all snapshots is consistent with that depicted in Fig. 1(a).

terpenetrate and coalesce into a three-dimensional perforated lamellar network (Fig. 4j). This interconnected architecture suppresses strain localization and enables distributed load sharing, stabilizing the stress plateau. Remarkably, strain hardening emerges before failure, during which the perforated network undergoes dynamic reorganization-proliferating lamellar segments while preserving global connectivity. This adaptive reconstruction redistributes mechanical loads across multiple pathways, accounting for the observed hardening behavior. When strain exceeds the network's capacity, lamellar rupture and void nucleation commence (inset, Fig. 4k). Progressive void expansion ultimately dismantles the network architecture, precipitating failure (inset, Fig. 4l). The highly polydisperse system (PDI=1.8) initiates with a pre-

formed perforated lamellar structure (Fig. 4n), circumventing the lamellar-to-perforated transition observed at PDI=1.5 (Figs. 4o–4r). Its stress-strain profile (Fig. 4m) mirrors that of PDI=1.5 but exhibits elevated stress levels and enhanced strain hardening, attributable to the superior connectivity of the initial perforated network. Analysis of the order parameter (P_2) further supports these observations, revealing distinct structural evolution trends for low- and high-PDI systems (see Fig. S4 in ESI for details).

To further unravel the PDI-induced mechanical response at molecular level, we analyzed chain conformations of each system. When $n > 1$, the flexible C blocks may undergo stretching or collapsing during phase separation, causing the two R blocks connected by a C block to adopt one of two distinct spatial distributions (Fig. 5a): (i) when the C block stretches, the two R blocks are located in adjacent R domains, forming a bridging conformation; (ii) when the C block collapses, the two R blocks are located in the same R domain, forming a looping conformation. Bridging conformations form robust molecular networks that effectively connect distinct domains, and are thus expected to contribute significantly to the mechanical properties of the polymer.[37–39] To investigate the influence of PDI on the formation of bridging conformations, we calculated the bridging fraction, ν_{bridge}, for the $(R_6C_6)_n$ and $(R_8C_8)_n$ systems with varying PDI values. Here, ν_{bridge} is defined as the ratio of the number of bridging conformations to the total number of bridging and looping conformations, *i.e.*, $\nu_{bridge} = N_B/(N_B + N_L)$. The distinction between these two conformations was based on spatial geometric criteria.[45] As shown in Fig. 5(a), two vectors, v_1 and v_2, are constructed to point from the center of mass of the C block (taken as the origin) to the centers of mass of the two terminal R blocks. The angle φ between these two vectors is used to classify the conformations: if $\varphi > 90^\circ$ (*i.e.*, $\cos\varphi < 0$), the C block is classified as a bridging conformation; if $\varphi \le 90^\circ$ (*i.e.*, $\cos\varphi \ge 0$), the C block is classified as a looping conformation. As shown in Fig. 5(b), increasing PDI raises ν_{bridge} for the $(R_6C_6)_n$ and $(R_8C_8)_n$ systems in their equilibrium self-assembled structures, but the specific trends exhibit notable differences. In the $(R_6C_6)_n$ system, ν_{bridge} increases nearly linearly with PDI, from about 0.27 at PDI=1.1 to about 0.40 at PDI=1.8. By contrast, for the $(R_8C_8)_n$ system, the rise is steeper at low PDI and levels off earlier, reaching about 0.38–0.39 beyond PDI ≈ 1.5–1.6. These trends stem from the fact that PDI and the parameter k modulate the statistical weights of bridging versus looping conformations of the C blocks by altering their relative conformational-entropy penalties. In particular, a single C block can adopt a bridging conformation only if 1. It stretches normal to the lamellar plane so as to span the full thickness of one C lamella; and 2. it undergoes a slight spatial and angular adjustment at the C–R junction (a "minor junction rearrangement") to ensure a smooth orientational match with the neighboring R segments. On the other hand, adopting a looping conformation involves three classes of penalties: 1. hairpin turns or intralamellar bending near the interface; 2. local crowding and orientational frustration arising from confining the two R blocks linked by a C block to the same R lamella; and 3. a chain-level registry cost: an interior loop breaks the ideal R|C|R|C stacking of chains across the lamellae, so surrounding segments must stretch or compress to restore perfect layer registry. At fixed k and l, PDI does not materially change the C lamella thickness or the ability of C blocks to span it; hence the baseline entropic cost of a bridging conformation is almost PDI-independent in our systems. Increasing PDI, however, redistributes mass toward longer chains and thereby increases the fraction of interior C blocks whose loops incur the larger chain-level registry cost. With the bridge cost unchanged, this reweighting favors bridging conformations, yielding the observed increase in ν_{bridge} with PDI (Fig. 5b). Higher k modulates this balance further. For the $(R_8C_8)_n$ system, the longer R blocks promote more highly ordered packing, which raises the conformational entropy cost of loops—especially from local crowding and orientational frustration, and chain-level registry repair. By contrast, the baseline lamellar-normal spanning cost of a bridge remains approximately constant, as its geometric commensurability is preserved through a proportional increase in the C lamella thickness and the C block contour length. This relative reduction in the entropic cost of bridges manifests more rapidly and saturates earlier for $k = l = 8$, consistent with the early plateau in Fig. 5(b). Nevertheless, while ν_{bridge} increases with PDI, it remains below 0.5, in agreement with theoretical predictions.[46] This reflects the intrinsic anisotropy of the lamellar phase and the associated entropic bias: the C block is confined in the lamellar-normal direction but relatively unconstrained in-plane, so loops can be realized locally by intralamellar bending or short hairpin turns, whereas bridges require a normal span across the C lamella. Consequently, loops possess a larger microstate count and are statistically favored. An auxiliary quantitative correlation can be observed between ν_{bridge} and the emergence of PL in the $(R_6C_6)_n$ system. Specifically, the morphology remains Lam at

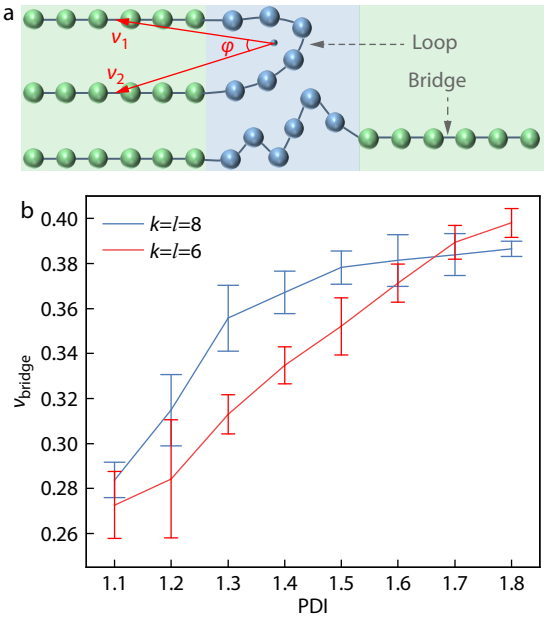

Fig. 5 (a) Schematic of the looping and bridging configurations of coil blocks. (b) shows the bridging fraction of coil blocks (ν_{bridge}) as a function of PDI for the $(R_6C_6)_n$ and $(R_8C_8)_n$ systems. Error bars represent standard deviations from five independent simulations.

https://doi.org/10.1007/s10118-026-3626-5

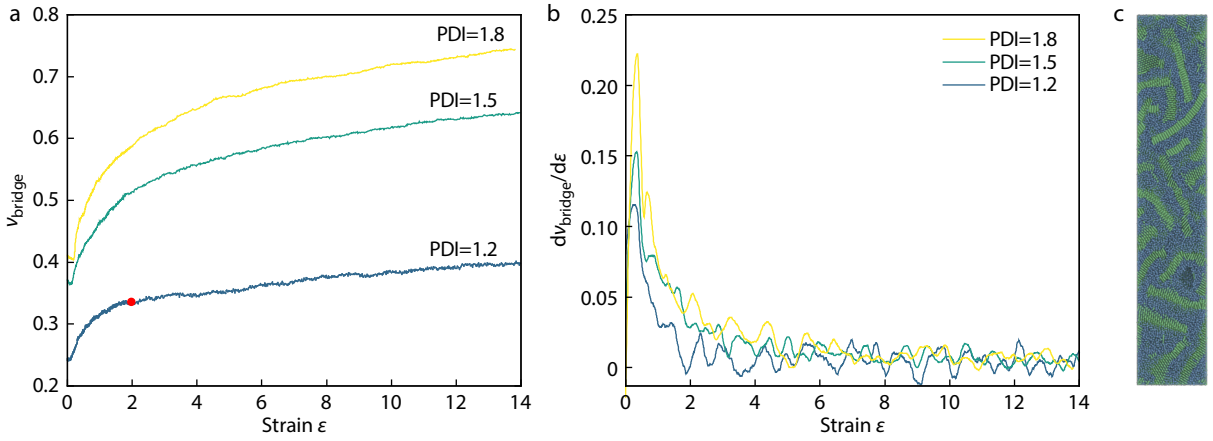

Fig. 6 (a) Evolution of ν_{bridge} during the tensile deformation process of $(R_6C_6)_n$ systems with PDI values of 1.2, 1.5, and 1.8; (b) The rate of change of ν_{bridge} with respect to strain ($d\nu_{bridge}/d\varepsilon$); (c) A simulation snapshot corresponding to the state marked by the red dot in panel (a).

PDI=1.6 ($\nu_{bridge} \approx 0.37$), whereas PL appears at PDI=1.7 ($\nu_{bridge} \approx 0.39$). Thus, for $(R_6C_6)_n$ system, the emergence of PL coincides with ν_{bridge} increasing to the about 0.37–0.39 range. This correspondence is not universal across different k values: for $(R_8C_8)_n$, ν_{bridge} reaches about 0.38–0.39 at PDI≥1.5 while the morphology remains Lam within the studied range. Taken together, these results indicate that, even when PDI produces only minor changes in the phase structure, the detailed molecular structures are still modulated.

We therefore tracked the evolution of ν_{bridge} during tensile deformation (Fig. 6). At large strains, initially sharp domain boundaries gradually become diffuse due to structural reorganization.

The evolution of ν_{bridge} reveals the dynamic molecular-scale load-bearing behavior. As shown in Fig. 6(a), ν_{bridge} evolution strongly depends on PDI and exhibits two distinct response modes.

Low PDI systems: systems with low polydispersity display limited bridge formation capacity. The PDI=1.0 system, composed entirely of diblock copolymers, inherently lacks bridge conformations, with ν_{bridge} remaining zero throughout deformation. For PDI=1.2, ν_{bridge} remains measurably low across the entire strain range. When $\varepsilon > 2$, lamellae disappear due to reassembly during tensile deformation (Fig. 6c), rendering bridging ill-defined at these strains. However, we can still track the fraction of chains with rigid segments oriented nearly parallel (angle about π)—beyond this strain, ν_{bridge} effectively measures chain alignment along the tensile direction.

In the small-strain regime, the modest increase in ν_{bridge} proves insufficient for stress redistribution, destabilizing the flat lamellae and causing pronounced stress softening. During this process, lamellae undergo significant twisting and fragmentation. Throughout the subsequent stress plateau, ν_{bridge} growth is nearly suppressed (as indicated by $d\nu_{bridge}/d\varepsilon$ in Fig. 6b), suggesting that the loop → bridge conformational transition is severely hindered. Consequently, no continuous, progressively reinforcing load-bearing network develops. Instead, structural evolution follows a heterogeneous, discontinuous pathway, manifesting as stress-strain oscillations that ultimately lead to microvoiding and material failure.

High PDI systems: for systems with large polydispersity (PDI=1.5 and 1.8), the molecular response shifts to a dynamic network-strengthening mode. These systems exhibit higher initial ν_{bridge} values and sustained growth throughout deformation. During early deformation stages, rapid loop → bridge transitions densify the load-bearing network, supporting the reconstructive structural evolution pathway (lamellae → perforated lamellae transition or perforated lamellae strengthening) and accounting for the milder strain softening observed previously.

Upon entering the intermediate-to-large strain regime, ν_{bridge} increases steadily, indicating continuous evolution of the load-bearing network. This process is PDI-dependent: higher PDI values yield steeper ν_{bridge} increases, as shown in Fig. 6(b). Notably, the PDI=1.8 system exhibits a distinct failure mechanism. Despite early microvoid formation due to the broad molecular weight distribution, enhanced reassembly capabilities enable structural reconstruction during tensile deformation. This maintains the final breaking strain while introducing significant structural reassembly, resulting in an additional strain hardening–softening cycle between $9 < \varepsilon < 12$.

CONCLUSIONS

In summary, we systematically investigated the impact of MWD, quantified by PDI, on the structural and mechanical performance of CP-FSs using a combined DPD and CGMD simulation framework. Our findings demonstrate that PDI plays a crucial role in determining domain connectivity. Specifically, for intermediate rigid segment lengths, packing frustration in high-PDI systems induces a structural transition from lamellae to perforated lamellae. At the molecular level, increasing PDI significantly elevates ν_{bridge}, establishing a robust load-bearing network that enhances both yield strength and yield strain. Furthermore, the accelerated growth of ν_{bridge} in high-PDI systems fundamentally alters the structural evolution pathway during tensile deformation—from the destructive fibrillation observed in low-PDI systems to the reconstructive formation or strengthening of perforated lamellae. This process not only induces pronounced strain hardening but also preserves a continuous domain morphology even at large strains. Given that such connectivity is essential for stable charge-transport pathways in

https://doi.org/10.1007/s10118-026-3626-5

various high-performance photovoltaics,[47–49] it is expected to improve the strain resistance of the material's photovoltaic performance. These findings emphasize that controlled MWD represents a powerful, composition-independent strategy for engineering mechanically resilient active layers. This work provides essential insights for the rational design of FOSCs, offering a pathway to simultaneously enhance photovoltaic efficiency and mechanical durability.

Conflict of Interests

The authors declare no interest conflict.

Electronic Supplementary Information

Electronic supplementary information (ESI) is available free of charge in the online version of this article at http://doi.org/10.1007/s10118-026-3626-5.

Data Availability Statement

The data that support the findings of this study are available from the corresponding author upon reasonable request. The author's contact information: luzhy@jlu.edu.cn.

ACKNOWLEDGMENTS

This work was financially supported by the National Natural Science Foundation of China (No.22133002).

REFERENCES

1 Li, S.; Li, Z.; Wan, X.; Chen, Y. Recent progress in flexible organic solar cells. *eScience* **2023**, *3*, 100085.
2 Wang, D.; Liu, H.; Li, Y.; Zhou, G.; Zhan, L.; Zhu, H.; Lu, X.; Chen, H.; Li, C. Z. High-performance and eco-friendly semitransparent organic solar cells for greenhouse applications. *Joule* **2021**, *5*, 945–957.
3 Zhu, J.; Xia, J.; Li, Y.; Li, Y. Perspective on flexible organic solar cells for self-powered wearable applications. *ACS Appl. Mater. Interfaces* **2025**, *17*, 5595–5608.
4 Song, W.; Ye, Q.; Chen, Z.; Ge, J.; Xie, L.; Ge, Z. Advances in stretchable organic photovoltaics: flexible transparent electrodes and deformable active layer design. *Adv. Mater.* **2024**, *36*, 2311170.
5 Yang, F.; Huang, Y.; Li, Y.; Li, Y. Large-area flexible organic solar cells. *npj Flex. Electron.* **2021**, *5*, 30.
6 Yan, Y.; Duan, B.; Ru, M.; Gu, Q.; Li, S.; Zhao, W. Toward flexible and stretchable organic solar cells: a comprehensive review of transparent conductive electrodes, photoactive materials, and device performance. *Adv. Energy Mater.* **2025**, *15*, 2404233.
7 Park, J. S.; Kim, G. U.; Lee, S.; Lee, J. W.; Li, S.; Lee, J. Y.; Kim, B. J. Material design and device fabrication strategies for stretchable

Graphical Abstract

Molecular Weight Distribution Effects on the Structural and Mechanical Performance of Conjugated Polymers Incorporating Flexible Spacers: A Simulation Study

Hai-Yan Weng, Ji-Yuan Xing, Rui Shi, and Zhong-Yuan Lu

Jilin University; Changchun Institute of Applied Chemistry, Chinese Academy of Sciences

This work demonstrates that molecular weight distribution, quantified by the polydispersity index (PDI), governs structure-property relationships in conjugated polymers incorporating flexible spacers. Increasing PDI promotes a loop-to-bridge conformational transition, transforming lamellar phase to perforated lamellar phase at intermediate rigid-segment lengths, switching deformation from destructive fibrillation to reconstructive strengthening, and enhancing both yield strength and strain.

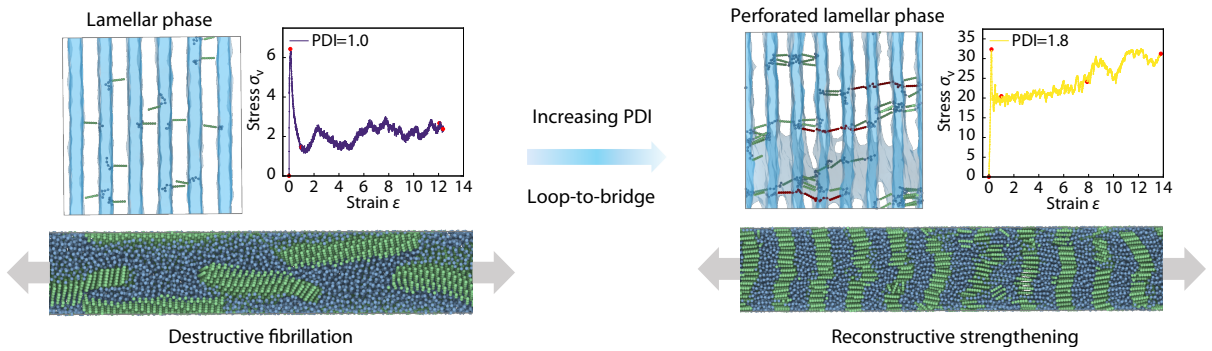

Chinese J. Polym. Sci. 2026, 44, 2331–2340 *https://doi.org/10.1007/s10118-026-3626-5*

organic solar cells. *Adv. Mater.* **2022**, *34*, 2201623.
8 Mitchell, V.; Jones, D. Advances toward the effective use of block copolymers as organic photovoltaic active layers. *Polym. Chem.* **2018**, *9*, 795–814.
9 Zhou, H.; Yang, L.; You, W. Rational design of high performance conjugated polymers for organic solar cells. *Macromolecules* **2012**, *45*, 607–632.
10 Qiu, Z.; Hammer, B. A.; Müllen, K. Conjugated polymers–Problems and promises. *Prog. Polym. Sci.* **2020**, *100*, 101179.
11 Lee, Y.; Gomez, E. D. Challenges and opportunities in the development of conjugated block copolymers for photovoltaics. *Macromolecules* **2015**, *48*, 7385–7395.
12 Xie, R.; Colby, R. H.; Gomez, E. D. Connecting the mechanical and conductive properties of conjugated polymers. *Adv. Electron. Mater.* **2018**, *4*, 1700356.
13 Zuo, J.; Han, D.; Yao, H.; Kuvondikov, V.; Ye, L. Stretching the future: strategies and emerging trends in stretchable organic photovoltaic materials. *Energy Environ. Sci.* **2025**, *18*, 6344–6365.
14 Zheng, Y.; Zhang, S.; Tok, J. B. H.; Bao, Z. Molecular design of stretchable polymer semiconductors: current progress and future directions. *J. Am. Chem. Soc.* **2022**, *144*, 4699–4715.
15 Root, S. E.; Savagatrup, S.; Printz, A. D.; Rodriquez, D.; Lipomi, D. J. Mechanical properties of organic semiconductors for stretchable, highly flexible, and mechanically robust electronics. *Chem. Rev.* **2017**, *117*, 6467–6499.
16 Genene, Z.; Lee, J. W.; Lee, S. W.; Chen, Q.; Tan, Z.; Abdulahi, B. A.; Yu, D.; Kim, T. S.; Kim, B. J.; Wang, E. Polymer acceptors with flexible spacers afford efficient and mechanically robust all-polymer solar cells. *Adv. Mater.* **2022**, *34*, 2107361.
17 Chen, Q.; Han, Y. H.; Franco, L. R.; Marchiori, C. F.; Genene, Z.; Araujo, C. M.; Lee, J. W.; Phan, T. N. L.; Wu, J.; Yu, D. Effects of flexible conjugation-break spacers of non-conjugated polymer acceptors on photovoltaic and mechanical properties of all-polymer solar cells. *Nano-Micro Lett.* **2022**, *14*, 164.
18 Luo, X.; Freychet, G.; Gan, Z.; An, K.; Du, H.; Wang, C.; Li, N.; Zhong, W.; Ying, L. Intrinsically stretchable organic photovoltaic thin films enabled by optimized donor–acceptor pairing. *Macromolecules* **2023**, *56*, 8928–8938.
19 Ye, Q.; Chen, Z.; Yang, D.; Song, W.; Zhu, J.; Yang, S.; Ge, J.; Chen, F.; Ge, Z. Ductile oligomeric acceptor-modified flexible organic solar cells show excellent mechanical robustness and near 18% efficiency. *Adv. Mater.* **2023**, *35*, 2305562.
20 Wang, H.; Kou, H.; Pan, J.; Wang, X.; Liu, D.; Yang, R. Design high-performance stretchable light-harvesting polymers for organic solar cells *via* synergistic effect of flexible alkyl segment and hydrogen bond. *Small* **2025**, *21*, 2412767.
21 Rahmanudin, A.; Yao, L.; Sivula, K. Conjugation break spacers and flexible linkers as tools to engineer the properties of semiconducting polymers. *Polym. J.* **2018**, *50*, 725–736.
22 Ding, Z.; Liu, D.; Zhao, K.; Han, Y. Optimizing morphology to trade off charge transport and mechanical properties of stretchable conjugated polymer films. *Macromolecules* **2021**, *54*, 3907–3926.
23 Zhu, J.; Yan, C.; Wang, J.; Li, H.; Cheng, P. Control of molecular aggregation structures towards flexible organic photovoltaics. *Mater. Horiz.* **2025**, *12*, 6069–6081.
24 Lee, J. W.; Sun, C.; Lee, S. W.; Kim, G. U.; Li, S.; Wang, C.; Kim, T. S.; Kim, Y. H.; Kim, B. J. Sequentially regular polymer acceptors featuring flexible spacers for high-performance and mechanically robust all-polymer solar cells. *Energy Environ. Sci.* **2022**, *15*, 4672–4685.
25 Seo, S.; Lee, J. W.; Kim, D. J.; Lee, D.; Phan, T. N. L.; Park, J.; Tan, Z.; Cho, S.; Kim, T. S.; Kim, B. J. Poly (dimethylsiloxane)-block-PM6 polymer donors for high-performance and mechanically robust polymer solar cells. *Adv. Mater.* **2023**, *35*, 2300230.
26 Lee, J. W.; Jeong, D.; Kim, D. J.; Phan, T. N. L.; Park, J. S.; Kim, T. S.; Kim, B. J. Flexible-spacer incorporated polymer donors enable superior blend miscibility for high-performance and mechanically-robust polymer solar cells. *Energy Environ. Sci.* **2021**, *14*, 4067–4076.
27 Ding, Z.; Hua, J.; Gao, Z.; Wang, M.; Zhao, K.; Han, Y. Molecular weight optimization for intrinsically stretchable conjugated polymers: from film microstructure to strain-insensitive performance. *J. Mater. Chem. C* **2025**, *13*, 12612–12627.
28 Ismail Saqib, M.; Yin, X.; Liu, Z.; Zhao, M.; Cheng, M.; Li, Y.; Song, C.; Liang, Q.; Xin, J.; Miao, Z. The effects of polymer molecular weight on morphology and the device efficiency: progress and prospects for organic solar cells. *Macromol. Chem. Phys.* **2025**, *226*, 2500031.
29 Lee, H. G.; Lee, J. W.; Oh, E. S.; Lee, M. J.; Kim, T. S.; Lee, C.; Kim, B. J. The effect of rigid-block length in elastomer-containing photoactive block copolymers on the photovoltaic and mechanical properties of polymer solar cells. *J. Mater. Chem. A* **2024**, *12*, 19039–19051.
30 Liang, Z.; Neshchadin, A.; Zhang, Z.; Zhao, F. G.; Liu, X.; Yu, L. Stille polycondensation: a multifaceted approach towards the synthesis of polymers with semiconducting properties. *Polym. Chem.* **2023**, *14*, 4611–4625.
31 Tian, D.; Wang, J.; Huang, X.; Ding, Y.; Hu, A. Understanding broad polydispersity in step-growth polymerization *via* catalyst competition mechanism. *Chinese J. Polym. Sci.* **2024**, *42*, 1897–1904.
32 Shin, W.; Ko, W.; Jin, S. H.; Earmme, T.; Hwang, Y. J. Reproducible and rapid synthesis of a conjugated polymer by Stille polycondensation in flow: Effects of reaction parameters on molecular weight. *Chem. Eng. J.* **2021**, *412*, 128572.
33 Caddeo, C.; Ackermann, J.; Mattoni, A. A theoretical perspective on the thermodynamic stability of polymer blends for solar cells: From experiments to predictive modeling. *Solar RRL* **2022**, *6*, 2200172.
34 Li, Z.; Tolba, S. A.; Wang, Y.; Alesadi, A.; Xia, W. Modeling-driven materials by design for conjugated polymers: insights into optoelectronic, conformational, and thermomechanical properties. *Chem. Commun.* **2024**, *60*, 11625–11641.
35 Gao, H.; Yu, Z.; Zhang, X.; Yu, X.; Xing, J.; Zhu, Y.; Qian, H. J.; Lu, Z. Y. A mini review of the recent progress in coarse-grained simulation of polymer systems. *Chin. J. Struct. Chem.* **2024**, *43*, 100266.
36 Flory, P. J. Molecular size distribution in linear condensation polymers. *J. Am. Chem. Soc.* **1936**, *58*, 1877–1885.
37 Chu, X.; Xu, Z.; Cao, Y. C.; Li, W. Simulation study on the mechanical properties of lamella-forming ABABA linear multiblock copolymers. *Macromolecules* **2024**, *57*, 9536–9545.
38 Xu, Z.; Chu, X.; Li, W. Microscopic origins of the distinct mechanical response of ABA and ABC block copolymer nanostructures. *ACS Macro Lett.* **2024**, *13*, 240–246.
39 Chen, T.; Xu, Z.; Chu, X.; Peng, L.; Huang, X.; Li, W. A simulation study on the effect of tailoring molecular architectures on the mechanical behaviors of lamella-forming BABCB linear multiblock copolymers. *Macromolecules* **2025**, *58*, 6387–6398.
40 Stukowski, A. Visualization and analysis of atomistic simulation data with OVITO–the Open Visualization Tool. *Model. Simul. Mater. Sci. Eng.* **2009**, *18*, 015012.
41 Zhu, Y. L.; Liu, H.; Li, Z. W.; Qian, H. J.; Milano, G.; Lu, Z. Y. GALAMOST: GPU-accelerated large-scale molecular simulation toolkit. *J. Comput. Chem.* **2013**, *34*, 2197–2211.
42 Xu, J.; Guo, S.; Zhen, M.; Yu, Z.; Zhu, Y.; Milano, G.; Lu, Z. PyGAMD: python graphics processing unit-accelerated molecular dynamics software. *Mater. Genome Eng. Adv*. **2025,** e70019.
43 Matsen, M. W. Polydispersity-induced macrophase separation in diblock copolymer melts. *Phys. Rev. Lett.* **2007**, *99*, 148304.

44 Kim, I.; Li, S. Recent progress on polydispersity effects on block copolymer phase behavior. *Polym. Rev.* **2019**, *59*, 561–587.
45 Li, S.; Li, K.; Xu, Q.; Wang, Y.; Yu, C.; Zhou, Y. Solution self-assembly behavior of rod-alt-coil alternating copolymers *via* simulations. *Phys. Chem. Chem. Phys.* **2019**, *21*, 25148–25157.
46 Matsen, M. Bridging and looping in multiblock copolymer melts. *J. Chem. Phys.* **1995**, *102*, 3884–3887.
47 Rasool, S.; Yeop, J.; Cho, H. W.; Lee, W.; Kim, J. W.; Yuk, D.; Kim, J. Y. Path to the fabrication of efficient, stable and commercially viable large-area organic solar cells. *Mater. Futures* **2023**, *2*, 032102.
48 Yu, W.; Zou, Y.; Zhang, S.; Liu, Z.; Wu, C.; Qu, B.; Chen, Z.; Xiao, L. Carbon-based perovskite solar cells with electron and hole-transporting/-blocking layers. *Mater. Futures* **2023**, *2*, 022101.
49 Zhang, L.; Wang, Y.; Meng, X.; Zhang, J.; Wu, P.; Wang, M.; Cao, F.; Chen, C.; Wang, Z.; Yang, F. The issues on the commercialization of perovskite solar cells. *Mater. Futures* **2024**, *3*, 022101.